Systematics of x-ray resonant scattering amplitudes in $R\mathrm{Ni}_2\mathrm{Ge}_2$ (R=Gd,Tb,Dy,Ho,Er,Tm): The origin of the branching ratio at the L edges of the heavy rare earths

J. W. Kim, Y. Lee, D. Wermeille, B. Sieve, L. Tan, S. L. Bud'ko, S. Law, P. C. Canfield, B. N. Harmon, and A. I. Goldman*
Ames Laboratory, USDOE and the Department of Physics and Astronomy, Iowa State University, Ames, Iowa 50011, USA
(Received 13 April 2005; revised manuscript received 8 June 2005; published 1 August 2005)

An investigation of the x-ray resonant magnetic scattering (XRMS) across the series of heavy rare-earth elements, coupled with first-principles calculations, has revealed that spin-orbit coupling in the 5*d* band plays a critical role in the systematics of the XRMS and x-ray magnetic circular dichroism branching ratio at the *L* edges of magnetic rare-earth compounds.

DOI: 10.1103/PhysRevB.72.064403 PACS number(s): 78.70.Ck, 61.10.Dp, 78.70.En

Magnetic x-ray scattering and spectroscopy techniques, such as x-ray resonant magnetic scattering (XRMS) and x-ray magnetic circular dichroism (XMCD), have become valuable tools for the study of magnetic materials.[1] XMCD in particular has become a powerful technique that, when combined with sum rules derived from an atomic model, yields direct information about orbital specific spin and orbital moments.[2,3] These sum rules are rather accurate when applied to solids containing transition metals, and their applicability has been confirmed for solids by band-structure calculations.[4] Unfortunately the same sum rules for the L_2 and L_3 absorption edges in rare-earth materials do not work. Further investigations of the systematics and underlying physics of XRMS and XMCD at the rare-earth L_2 and L_3 edges are required.

XRMS and XMCD are closely related, both arising from electronic transitions between core levels to higher lying empty orbitals at the x-ray absorption edges of magnetic ions. There remain, however, several unresolved issues concerning the details and systematics of the resonant scattering amplitudes in rare-earth compounds.[4] At the L edges of the rare-earth elements, these processes primarily involve electric dipole transitions ($E1$) from the $2p_{1/2}$ (L_2 edge) and $2p_{3/2}$ (L_3 edge) core levels to the empty 5*d* states. Unlike nonresonant magnetic x-ray scattering, where the intensity of magnetic diffraction peaks can be related directly to the spin and orbital magnetization density of the 4*f* electrons, XRMS measurements of rare-earth L_2 and L_3 edges probe magnetic order through the spin polarization of the 5*d* states. Therefore, they can be influenced by a number of factors, including the exchange interaction with the partially filled 4*f* shell, spin-orbit coupling (SOC), band structure, and crystal-electric field effects. Information about the 5*d* electrons is important because they play such essential roles in coupling the 4*f* moments with each other [the Ruderman-Kittel-Kasuya-Yosida (RKKY) mechanism], which results in the often exotic magnetic structures exhibited by rare-earth materials.

Deciphering the information contained in XMCD and XRMS amplitudes, and relating these amplitudes to the details of the electronic and magnetic structure of the material, are important, but difficult tasks. Over the past few years, one of the most intriguing issues has been the so-called branching ratio problem in the rare-earth elements.[1] Measurements of the ratio of the L_3/L_2 resonant scattering intensity consistently show that the L_3 edge intensities are significantly larger than the corresponding L_2 edge intensities for the heavy rare-earth elements, whereas the inverse is true for the light rare earths. Since the resonant scattering cross section and the XMCD amplitude are closely related, the same trend is observed in the relative amplitudes of XMCD measurements at the L_2 and L_3 edges of rare-earth compounds.

Spin-polarized band-structure calculations that include *only* the 4*f*-5*d* exchange interaction (no conduction-band SOC or 4*f* orbital polarization), produce a branching ratio across the entire rare-earth series equal to unity (1:1 for XRMS and 1:−1 for XMCD). Atomic models,[5,6] with parametrized 5*d* orbitals, have met with some success in explaining the branching ratios observed in the $R_2\mathrm{Fe}_{17}$ series, for example, by including 4*f* orbital polarization and introducing "breathing" (a contraction of the spin-up radial function relative to the spin-down radial function) of the 5*d* orbitals. This increases the overlap of the 5*d* spin-up states with the 2*p* core states, as shown by Harmon and Freeman.[7] Being primarily atomic models, however, they do not include the strong dependence of the radial functions on band energies. Indeed, the 4*f*-5*d* exchange energy corresponding to the bonding and antibonding 5*d* states differs by more than a factor of 2. By neglecting solid-state effects, not only do the atomic models incorrectly incorporate the 5*d* radial dependence on band energy, but this error is amplified in the 2*p* to 5*d* optical matrix elements and cannot be corrected by implementing a single so-called "breathing" parameter of the atomic models, introduced to model the differences between spin-up and spin-down radial functions (with no energy dependence).

The atomic models, when trying to describe the L_3 and L_2 branching ratio for the dichroic spectra, also neglect spin-orbit coupling in the 5*d* final states, although it is well known that the L_3 and L_2 intensity for the *absorption edges* differ from the statistically expected 2:1 ratio because of the spin-orbit coupling in the 5*d* final states.[8] Nevertheless the atomic models have been able to produce the trend seen in the observed L_3/L_2 XMCD and XRMS branching ratios. The key ingredient in the atomic models that allows some success is the inclusion of 4*f*-5*d* multipole Coulomb interactions;[5] however, we find that these interactions are small compared to the solid-state effects (the 5*d* bands are 8 eV wide), and

are not responsible for the large variation in the L_3/L_2 ratio across the heavy rare-earth series. Indeed, until now the origin of the variation of the branching ratio in the heavy rare-earth compounds has remained problematical,[4] and the extension of current treatments of both XRMS and XMCD amplitudes to extract compound specific magnetic property information remains a priority.

Here, we take an important step in addressing this issue through a systematic study of the XRMS branching ratio at the L edges of heavy rare-earths in $R\mathrm{Ni}_2\mathrm{Ge}_2$ compounds ($\mathrm{ThCr}_2\mathrm{Si}_2$ structure, space group $I4/mmm$) for R=Gd through Tm. Our approach involves exploiting the fact that similarities in the chemistry of rare-earth elements across the series allow the easy substitution of one rare-earth element for another in isostructural compounds. Since the resonant scattering at each absorption edge is element specific, probing the systematics of resonant scattering associated with several different rare-earth elements is possible using only a few mixed rare-earth samples. This helps to reduce the uncertainty in the measurements arising from variations in quality and mosaic from sample to sample. Further, the relatively straightforward incommensurate antiferromagnetic structure found at low temperature in the $R\mathrm{Ni}_2\mathrm{Ge}_2$ family of compounds has been the subject of prior XRMS and single-crystal neutron scattering investigations[9] as well as polycrystalline neutron measurements.[10]

Our results concerning the branching ratio across the series are compared with dichroic amplitudes calculated for the hcp heavy rare-earth elements in the ferromagnetic state (for XMCD) using the self-consistent scalar relativistic full potential LAPW+U method, with SOC added as a perturbation. We show that by including SOC in the 5*d* states, the 1:1 branching ratio across the rare-earth series is dramatically changed, and brought into substantial agreement with experiment.

I. EXPERIMENTAL DETAILS

Single crystals of $[\mathrm{Gd}_{1/3}\mathrm{Er}_{1/3}\mathrm{Tm}_{1/3}]\mathrm{Ni}_2\mathrm{Ge}_2$ and $[\mathrm{Gd}_{1/4}\mathrm{Tb}_{1/4}\mathrm{Dy}_{1/4}\mathrm{Ho}_{1/4}]\mathrm{Ni}_2\mathrm{Ge}_2$ were produced at the Ames Laboratory using the high-temperature solution-growth technique.[11,12] The $R\mathrm{Ni}_2\mathrm{Ge}_2$ compounds order antiferromagnetically, via the indirect exchange (RKKY) interaction, below Néel temperatures (T_N) ranging from 1.5 K for Tm to 27.1 K for Gd.[12] The values of T_N for the mixed rare-earth samples used in this experiment were approximately 12 K for both compounds. The moderate value of T_N, together with the absence of additional magnetic transitions in the bulk susceptibility measurements of the samples is consistent with a random substitution of the rare-earth elements.

XRMS measurements were performed on the 6 ID-B beam line in the MUCAT Sector at the Advanced Photon Source. A liquid-nitrogen-cooled, double-crystal Si(111) monochromator and a bent mirror were used to select the incident photon energy, focus the beam, and suppress higher-order harmonics. The sample was mounted on a copper rod on the cold finger of a closed cycle displex refrigerator. All measurements were carried out at the base temperature of the displex, about 7 K. The sample, oriented so that the scattering plane of the experiment was coincident with the ($h0l$) zone, was encapsulated in a Be dome with a He exchange gas to enhance thermal transfer. The resonant scattering measurements were carried out with the incident radiation linearly polarized perpendicular to the scattering plane (σ polarization). In this geometry, only the component of the magnetic moment that is in the scattering plane will contribute to the resonant scattering arising from electric dipole transitions from the 2*p*-to-5*d* states. The linear polarization of the scattered radiation for dipole resonant scattering is parallel to the scattering plane (π polarization). A pyrolytic graphite analyzer PG(0 0 6), optimized to select primarily π-polarized radiation was used to reduce the background from charge scattering.

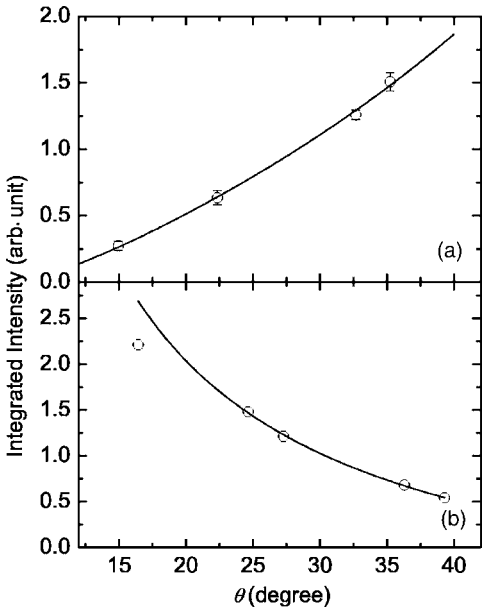

FIG. 1. Integrated intensities of (0 0 $L\pm\tau$) reflections measured at the Gd L_3 edge for (a) $[\mathrm{Gd}_{1/4}\mathrm{Tb}_{1/4}\mathrm{Dy}_{1/4}\mathrm{Ho}_{1/4}]\mathrm{Ni}_2\mathrm{Ge}_2$ and (b) $[\mathrm{Gd}_{1/3}\mathrm{Er}_{1/3}\mathrm{Tm}_{1/3}]\mathrm{Ni}_2\mathrm{Ge}_2$. The solid lines represent the fits to the data with $I=A(-z_1\cos\theta+z_3\sin\theta)^2/\sin 2\theta$, where A is a scaling factor, and z_1 and z_3 are the components of the magnetic moment unit vector along the **a** and **c** directions, respectively.

The antiferromagnetic ordering below T_N in the $R\mathrm{Ni}_2\mathrm{Ge}_2$ compounds is characterized by a wave vector of the form (0 0 τ_z), with τ_z ranging from about 0.75 to 0.81. For $[\mathrm{Gd}_{1/4}\mathrm{Tb}_{1/4}\mathrm{Dy}_{1/4}\mathrm{Ho}_{1/4}]\mathrm{Ni}_2\mathrm{Ge}_2$, below T_N, $\tau_z=0.752\pm0.001$. In Fig. 1(a) we show the results of measurements of the angular dependence[13] of the resonant scattering at the Gd L_3 edge indicating that the magnetic moment lies primarily along the c axis of the tetragonal structure, consistent with the axial anisotropy expected for the Tb, Dy, and Ho compounds.[12] For $[\mathrm{Gd}_{1/3}\mathrm{Er}_{1/3}\mathrm{Tm}_{1/3}]\mathrm{Ni}_2\mathrm{Ge}_2$, $\tau_z=0.759\pm0.001$ and the magnetic moment lies primarily within the basal plane [Fig. 1(b)] of the tetragonal structure, consistent with the planar anisotropy expected for the Er and Tm compounds.[12]

For each of the two samples, the XRMS intensity was recorded at all of the rare-earth L_2 and L_3 absorption edges over a range of approximately ±25 eV about the absorption edge energy. At each energy, the integrated intensity of the

magnetic satellite at $(0\ \ 0\ \ 6+\tau_z)$ was obtained with a rocking scan through the sample mosaic. The same procedure was used to obtain backgrounds for the energy spectra above the respective T_N for each sample. In order to extract and compare the resonant scattering intensities at the various edges, separated by several keV in energy, careful account must be taken of sample and beam line absorption factors over the entire energy range. These energy-dependent corrections were obtained through energy scans over the range of interest with powders of the two samples. In addition, the throughputs of the beam line optics and the polarization analyzer were measured over the entire energy range. For sample absorption corrections, small single crystal pieces were ground to prepare a fine powder sample. The powder was uniformly spread over Scotch tape and stacked to achieve approximately one absorption length at 8 keV. The transmission through the sample was measured for all relevant energy ranges. The same number of Scotch tape layers, without sample, were measured under the same conditions to remove the contribution of the Scotch tape itself. The energy-dependent absorption coefficient, $\mu(E)$ was used to correct the magnetic scattering intensity in each energy range. From the monitor (ion chamber) to the detector, the incident and scattered x-ray beam passes through various media including air, the Be windows of the vacuum beam paths, the Be domes of the cryostat, and the polarization analyzer. Furthermore, the response of the ion chamber, used as a monitor, and the efficiency of the polarization analyzer are energy dependent as well. Therefore, the throughput of the beam line was measured for all the relevant energy ranges, with the same configuration as for the scattering measurement, using the direct beam and correcting for the necessary attenuation of the beam (by Al), the polarization factor $\cos^2 2\theta_{\text{analyzer}}$, and the finite mosaic of the analyzer crystal (about 0.3°).

To derive the XRMS scattering intensity both resonant and nonresonant magnetic scattering contributions must be taken into account.[14] To determine the dipole resonant scattering amplitude, $E_0^2(F_{11}-F_{1-1})$,[15] the energy line shapes were fit with the following function:

$$|f(\omega)|^2 \propto \left| -\frac{\Gamma}{4}\left(\frac{m}{\hbar^2}\right)\frac{E_0^2(F_{11}-F_{1-1})}{(E_0-\hbar\omega)^2+\Gamma^2/4}M_{res} + i\left[\frac{1}{2}\left(\frac{m}{\hbar^2}\right)\frac{E_0^2(F_{11}-F_{1-1})(E_0-\hbar\omega)}{(E_0-\hbar\omega)^2+\Gamma^2/4}M_{res} - \frac{\hbar\omega}{mc^2}M_{nonres}\right]\right|^2, \quad (1)$$

where E_0 is the pole of the resonance, Γ is the total width of the excited state (about 4 eV), ω is the incident photon frequency, m is the electron mass, and M_{res} and M_{nonres} are the polarization matrices for resonant and nonresonant scattering, respectively.[16] Both M_{res} and M_{nonres} were fixed by the orientation of the magnetic moments with respect to the scattering plane and were determined in a measurement of the angle dependence of the magnetic scattering (Fig. 1). Interference between the resonant and nonresonant scattering terms lead to an asymmetry in the energy line shape as demonstrated in Figs. 2 and 3 for the L_2 and L_3 edge measurements of each sample. After fitting all resonant scattering profiles, the extracted value of $E_0^2(F_{11}-F_{1-1})$ at each absorption edge was squared (to represent a resonant scattering in-

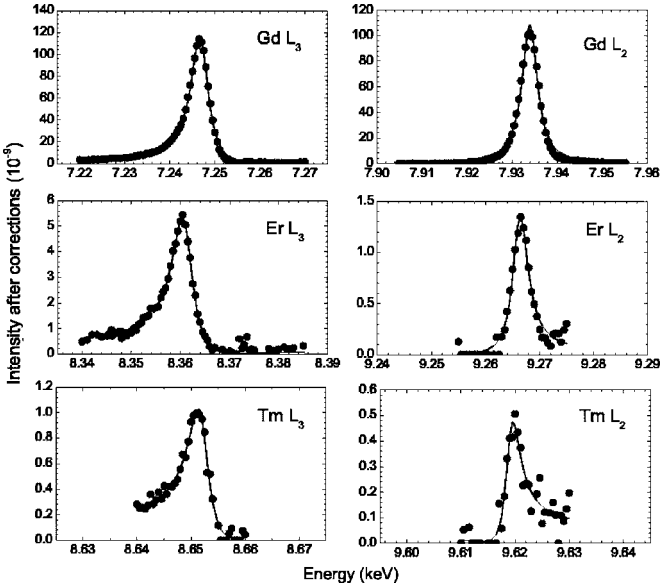

FIG. 2. XRMS energy scan through the rare-earth L_3 and L_2 edges for the $[Gd_{1/3}Er_{1/3}Tm_{1/3}]Ni_2Ge_2$ sample at the $(0\ \ 0\ \ 6+\tau_z)$ magnetic reflection. The solid lines represent the fits to the data as described in the text.

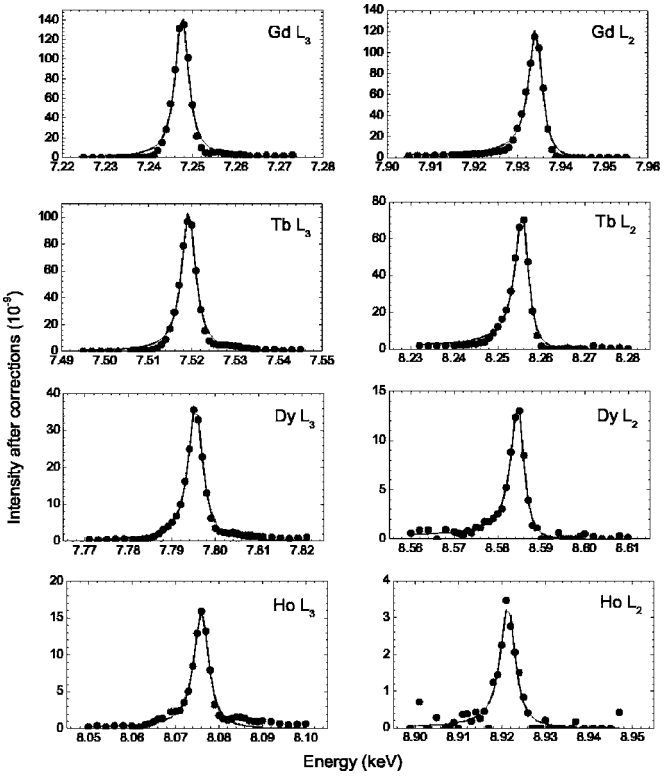

FIG. 3. XRMS energy scan through the rare-earth L_3 and L_2 edges for the $[Gd_{1/4}Tb_{1/4}Dy_{1/4}Ho_{1/4}]Ni_2Ge_2$ sample at the $(0\ \ 0\ \ 6+\tau_z)$ magnetic reflection. The solid lines represent the fits to the data as described in the text.

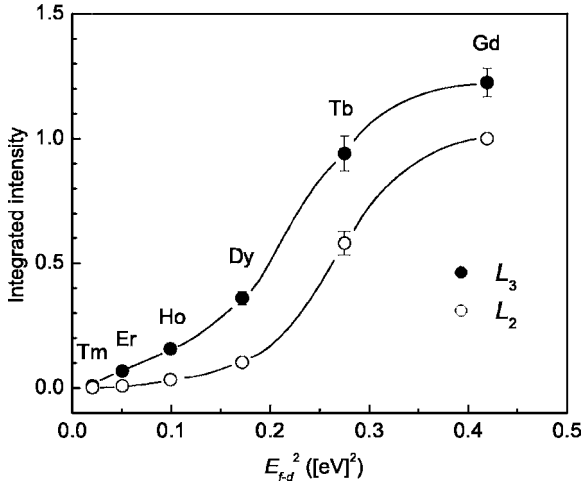

FIG. 4. The fit value of the integrated intensity of the resonant magnetic scattering, $E_0^4(F_{11}-F_{1-1})^2$, at the L_2 (open circles) and L_3 edges (closed circles) for both samples, plotted as a function of the square of the $4f$-$5d$ exchange energy (Ref. 17). The data are normalized to the integrated intensity at the Gd L_2 edge of the samples. The solid lines serve as a guide to the eye.

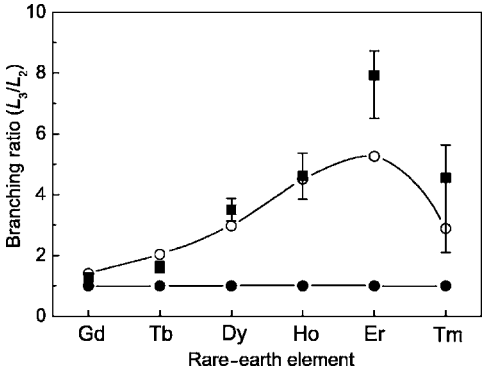

FIG. 5. The XRMS branching ratio for the heavy rare-earth elements in $R\mathrm{Ni}_2\mathrm{Ge}_2$ compounds. The solid squares represent the ratio of intensities from the L_2 and L_3 edges shown in Fig. 4. The solid circles show the result of the first-principles calculations, as described in the text, ignoring SOC in the $5d$ band. The open circles show the results of the same calculations, now including the effect of spin-orbit coupling in the $5d$ band.

tegrated intensity) and normalized to the value obtained at the Gd L_2 edge for each sample so that comparisons between samples could be made.

II. RESULTS

The importance of the $4f$-$5d$ exchange is highlighted in Fig. 4, where we plot the normalized XRMS integrated intensities at the L_2 and L_3 edges as a function of the square of the atomic $5d$ exchange energy splitting for the rare-earth elements.[17] There is a striking enhancement of the resonant scattering intensity as the $4f$-$5d$ exchange interaction increases from Tm to Gd, consistent with previous XMCD studies highlighting the importance of the $4f$-$5d$ exchange. In particular, for Gd, with seven unpaired $4f$ electrons, the on-site $4f$-$5d$ exchange interaction is largest and dominates over other interactions. Hence, we expect the L_2 and L_3 spectra for Gd to be only weakly affected by the specific crystalline environment. However, as one proceeds along the heavy rare-earth series the number of unpaired $4f$ electrons decreases, so that for Ho, Er, and Tm the $5d$ spin-orbit coupling and even the crystal-electric field interactions induce comparable, or greater, effects on the resonant scattering amplitude. Indeed, these rare-earth elements may provide useful probes of local environments if various sensitive features in the L_2 and L_3 spectra can be related to the fundamental interactions.

If the normalized integrated intensity of the magnetic scattering at the L_3 edge is divided by the normalized integrated intensity of the magnetic scattering at the L_2 edge, the branching ratio, plotted as solid squares in Fig. 5, is obtained. We note here that Eq. (1) does not explicitly include the contribution of quadrupole resonant scattering since attempts at fitting the data, with this term included, resulted in high correlations between the fitting parameters.[14] Nevertheless, we were able to estimate the resonant quadrupole contributions at each edge from atomic calculations[18] and found them to be negligible except for the Er L_3 ($<10\%$) and Tm L_3 ($<30\%$) spectra. The asymmetry in the error bars for Er and Tm in Fig. 3 reflect the quadrupole contributions in addition to the experimental error.

The trend observed in the branching ratio in Fig. 5 is consistent with prior XMCD studies.[5] While atomic models have found some success in reproducing this trend through the introduction of "breathing" and $4f$ orbital polarization, the role of SOC in the $5d$ band, and its effect on the branching ratio in the rare-earth elements has previously been neglected. Here, we include the SOC in first-principles spin-polarized band-structure calculations. Because the incommensurate ordering of the $R\mathrm{Ni}_2\mathrm{Ge}_2$ is problematic for band-structure techniques, we restricted ourselves to evaluating the magnetic ground state for the hcp heavy rare-earth elements in the ferromagnetic state (for XMCD). In this way we are missing some of the crystal-specific band-structure effects; however, the on-site $4f$-$5d$ exchange, the $5d$ radial function spin dependence, the solid-state bonding to antibonding radial dependence, and the SOC of the $5d$ bands are all nearly independent of crystal structure.

The details of the calculations are presented elsewhere,[19] and here we outline the main results. The spin-polarized scalar relativistic, self-consistent, full potential LAPW method was used for the calculations, employing the local-density approximation (LDA)+U approach to handle the localized $4f$ states. To isolate the effects of the SOC, calculations were performed with and without SOC, which was added in each iteration by the second variation method.[20] Also, to isolate the effect of the SOC to just the conduction bands, the $4f$ states were constrained (by choosing occupied m_l orbitals) to have zero angular momentum. This violates Hund's second rule for the $4f$ states, but still allows us to ascertain the effect of the strong $4f$-$5d$ exchange on the matrix elements. Actually, for the heavy rare-earth elements, the results were not affected significantly by relaxing this constraint, but since one atomic-based model suggested the strong branching ratio variation across the rare-earth elements arises from $4f$ orbital

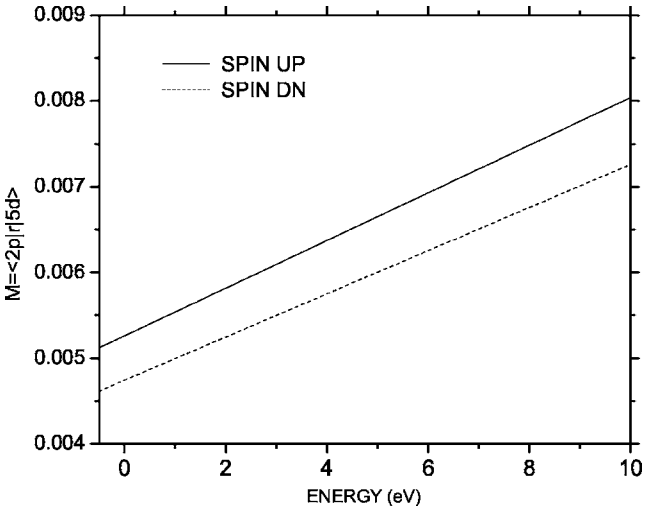

FIG. 6. Energy dependence of the radial dipole matrix elements for spin up (upper line) and spin down (lower line) for Gd. The Fermi energy E_F is located at 0.0 eV and the top of the 5*d* band is at approximately 8 eV. The matrix element is significantly larger for the antibonding states at the top of the 5*d* band.

polarization,[5] we decided to eliminate this interaction to demonstrate that the branching ratio is little influenced by the 4*f* orbital polarization.

We note that the exchange with 4*f* states is much larger for the higher unoccupied 5*d* states since their radial functions contract because of the antibonding nature of the highest energy levels. In Fig. 6 we show the resulting dependence of the radial dipole matrix elements, which is proportional to the XRMS amplitude or the XMCD dichroic amplitude, on the band energy. From this figure we see that the more localized states (antibonding) near the top of the 5*d* band (~8 eV) have a larger dipole matrix element with the 2*p* states and, hence, contribute more strongly to the XMCD and XRMS amplitudes. While this spin-dependence difference in the optical matrix elements of Fig. 6 is approximately accounted for in the atomic models[5] by the "breathing parameter," the dramatic change of the matrix elements with energy is not.

The magnitude of the SOC can be estimated for the 5*d* states from atomic calculations, which show the spin-orbit splitting between $5d_{3/2}$ and $5d_{5/2}$ states remains about 0.3 eV across the heavy rare-earth elements, while the 4*f*-5*d* exchange interaction (about 1 eV spin splitting at the Fermi level for Gd) scales with the number of unpaired 4*f* electrons. Thus, for Gd the exchange dominates, but for Er and Tm the spin-orbit interaction is comparable or even larger than the exchange splitting. The conduction-band states were used to calculate the XMCD spectra. The corresponding XRMS spectra were obtained from the XMCD spectra.[21] The calculated branching ratios both with (open circles) and without (filled circles) the inclusion of SOC in the conduction bands are shown in Fig. 5. In the absence of SOC, the branching ratio is exactly 1:1,[22] and with SOC, the branching ratio becomes comparable to the experimental values both in magnitude and trend. The theoretical results have also been normalized to the integrated intensity of the Gd L_2 edge.

While we have not dealt with the light rare-earth elements in this paper, preliminary calculations suggest that the L_3 dichroic intensities are strongly influenced by the unoccupied spin up 4*f* states hybridizing with the 5*d* energy bands. The observed small intensities of the light rare-earth L_3 dichroic spectra might be explainable by calculations that include a careful analysis of these effects.

In summary, through a systematic study of XRMS from the *L* edges of heavy rare-earth elements in RNi_2Ge_2 combined with first-principles calculations, we find that the observed branching ratio is primarily affected by the SOC in the 5*d* band. The trend across the heavy rare-earth series arises from the fact that the 4*f*-5*d* exchange interaction contribution to the resonant amplitudes decreases from Gd to Tm, allowing the spin-orbit contribution in the 5*d* band to take on a more important role.

ACKNOWLEDGMENTS

The authors would like to acknowledge the assistance of, and useful discussions with, C. Song, W. Good, Z. Islam, C. Detlefs, D. Robinson, and A. Kreyssig. MUCAT and the Ames Laboratory are supported by the Department of Energy, Office of Science under Contract No. W-7405-Eng-82. Use of the Advanced Photon Source is supported by the U.S. Department of Energy, Basic Energy Sciences, Office of Science, under Contract No. W-31-109-Eng-38.

*Corresponding author. Electronic mail: goldman@ameslab.gov

[1] See, for example, D. Gibbs, J. P. Hill, and C. Vettier, in *Third Generation Hard X-ray Sources: Source Properties, Optics, and Experimental Techniques*, edited by D. Mills (John Wiley and Sons, Inc., New York, 2002), p. 267.

[2] P. Carra, B. T. Thole, M. Altarelli, and X. Wang, Phys. Rev. Lett. **70**, 694 (1993).

[3] B. T. Thole, P. Carra, F. Sette, and G. van der Laan, Phys. Rev. Lett. **68**, 1943 (1992).

[4] C. Giorgetti, E. Dartyge, F. Baudelet, and R. M. Galera, Phys. Rev. B **70**, 035105 (2004).

[5] Michel van Veenendaal, J. B. Goedkoop, and B. T. Thole, Phys. Rev. Lett. **78**, 1162 (1997).

[6] K. Fukui, H. Matsuyama, I. Harada, J. C. Parlebas, and A. Kotani, J. Electron Spectrosc. Relat. Phenom. **104**, 67 (1999).

[7] B. N. Harmon and A. J. Freeman, Phys. Rev. B **10**, 1979 (1974); **10**, 4849 (1974).

[8] B. T. Thole and G. van der Laan, Phys. Rev. B **38**, 3158 (1988).

[9] Z. Islam, C. Detlefs, A. I. Goldman, S. L. Bud'ko, P. C. Canfield, J. P. Hill, Doon Gibbs, T. Vogt, and A. Zheludev, Phys. Rev. B **58**, 8522 (1998); Z. Islam, C. Detlefs, C. Song, A. I. Goldman, V. Antropov, B. N. Harmon, S. L. Bud'ko, T. Wiener, P. C.

Canfield, D. Wermeille, and K. D. Finkelstein, Phys. Rev. Lett. **83**, 2817 (1999); Z. Islam, C. Detlefs, A. I. Goldman, S. L. Bud'ko, P. C. Canfield, and A. Zheludev, Solid State Commun. **108**, 371 (1998).

[10] H. Pinto, M. Melamud, M. Kuznietz, and H. Shaked, Phys. Rev. B **31**, 508 (1985).

[11] P. C. Canfield and Z. Fisk, Philos. Mag. B **56**, 1117 (1992).

[12] S. L. Bud'ko, Z. Islam, T. A. Wiener, I. R. Fisher, A. H. Lacerda, and P. C. Canfield, J. Magn. Magn. Mater. **205**, 53 (1999).

[13] C. Detlefs, A. H. M. Z. Islam, A. I. Goldman, C. Stassis, P. C. Canfield, J. P. Hill, and D. Gibbs, Phys. Rev. B **55**, R680 (1997).

[14] D. Gibbs, G. Grübel, D. R. Harshman, E. D. Isaacs, D. B. McWhan, D. Mills, and C. Vettier, Phys. Rev. B **43**, 5663 (1991).

[15] J. P. Hannon, G. T. Trammell, M. Blume, and Doon Gibbs, Phys. Rev. Lett. **61**, 1245 (1988).

[16] J. P. Hill and D. F. McMorrow, Acta Crystallogr., Sect. A: Found. Crystallogr. **A52**, 236 (1996).

[17] The $4f$-$5d$ exchange energy was obtained as the splitting of equally occupied $5d$ spin-up and $5d$ spin-down states in a scalar-relativistic LSDA atomic calculation.

[18] X. Wang, T. C. Leung, B. N. Harmon, and P. Carra, Phys. Rev. B **47**, 9087 (1993).

[19] Y. Lee, J. W. Kim, A. I. Goldman, and B. N. Harmon, J. Appl. Phys. **97**, 10A311 (2005).

[20] D. D. Koelling and B. N. Harmon, J. Phys. C **10**, 3107 (1977).

[21] J. M. Tonnerre, L. Sève, D. Raoux, G. Soullié, B. Rodmacq, and P. Wolfers, Phys. Rev. Lett. **75**, 740 (1995).

[22] The exact 1:1 ratio is only obtained with the $2p_{3/2}$ and $2p_{1/2}$ radial functions being exactly the same. Using the actual radial functions for these core states results in about a 1% deviation from the 1:1 ratio.